15.2 A Dual-Doppler Analysis of a Nontornadic Supercell Observed on 12 June 2004 Using Ground-Based Doppler Radars

MARIO MAJCEN*, PAUL MARKOWSKI, AND YVETTE RICHARDSON

Department of Meteorology, Pennsylvania State University, University Park, PA

JOSHUA WURMAN

Center for Severe Weather Research, Boulder, CO

1. Introduction

Discriminating between tornadic and nontornadic supercells has been perhaps the leading motivation for the collection of field observations in and near supercell thunderstorms since the days of the Verification of the Origins of Rotation in Tornadoes Experiment (VORTEX). Mobile Doppler radars now somewhat routinely sample the low-level mesocyclone regions of supercells at close range, with sub-kilometer spatial resolution and temporal resolution on the order of 1–2 minutes or less, affording retrievals of the three-dimensional kinematic fields (when dual-Doppler observations are available) that enable analyses of supercells superior to those available from the fixed Doppler radar networks relied upon in the past (e.g., Ray et al. 1975; Brandes 1977, 1981).

The purpose of this paper is to present preliminary dual-Doppler observations of a nontornadic supercell sampled by a pair of Doppler on Wheels (DOW) radars (Wurman et al. 1997) on 12 June 2004 during the Radar Observations of Tornadoes and Thunderstorms Experiment (ROTATE). This case represents just one dual-Doppler dataset among many that now have been collected in supercells by ground-based mobile Doppler radars. It is hoped that the analysis of a large number of cases, one case at a time, might eventually allow us to identify recurring differences between tornadic and nontornadic supercells.

An overview of the dataset and analysis methods is given in section 2. Results are presented in section 3. Section 4 describes the tasks we will be undertaking in the upcoming months.

2. Data and methodology

On 12 June 2004, an outbreak of severe weather was spawned in association with a developing cyclone in the central Plains states. Several tornadoes were observed in supercells that were initiated along a dryline in south central Kansas, while other supercells, predominantly nontornadic, occurred farther north in southeastern Nebraska along and north of a warm front. Two DOW radars (DOW2 and DOW3) intercepted one of the nontornadic supercells in southern Nebraska near the town of Sprague. Although the supercell was nontornadic, it possessed strong low-level rotation. Maximum differential radial velocities (Δv_r) in excess of 35 m s^{-1} over a horizontal distance of 5–10 km were observed by the DOWs at an altitude of 1 km above ground level (AGL; hereafter all altitudes are AGL). Data collection started at 2203 UTC and ended at 2244 UTC, but the period of dual-Doppler observations of the mesocyclone region only extends from 2203 UTC until 2223 UTC, with a brief interruption between approximately 2217–2219 UTC.

The wavelength and the stationary, half-power beamwidth of both radars were 3 cm and 0.93°, respectively. Both radars collected data using a staggered pulse repetition frequency (PRF), which allowed for effective Nyquist velocities of 53.8 m s^{-1} (DOW2) and 98.9 m s^{-1} (DOW3). The DOWs were deployed along a north-south line, east of the mesocyclone center. The baseline was 8.4 km, which resulted in a dual-Doppler lobe having an area of approximately 220 km^2 (assuming that three-dimensional winds were to be trusted only if the interbeam angle was between 30°–150°).

Data from DOW2 and DOW3 were interpolated to a grid using a one-pass Barnes analysis (Barnes 1964) with an isotropic, spherical weight function and smoothing parameter, κ, of 0.15 km^2. The choice of this smoothing parameter yields a 25% theoretical response for features having a wavelength of 1.0 km, which is approximately 4 times the coarsest data spacing at a range of 17 km from the radars (approximately the coarsest data spacing in the dual-Doppler analysis region). The grid dimensions are 17×17×3 km , with a horizontal and vertical grid spacing of 100 m. An advection correction was incorporated into the analysis to account for the storm motion during the time required to complete a volume scan (roughly 60 seconds). The storm motion during the data collection had a zonal component of 8.4 m s^{-1} and a meridional component of 1.9 m s^{-1}.

The extrapolation of data to grid points was not permitted. The three-dimensional winds were retrieved by integrating the anelastic mass continuity equation upward from the ground, where vertical velocity was assumed to be zero. Because extrapolation was forbidden in the objective analysis stage, wind data were not retrieved at the lowest grid level ($z = 0$ m), and even at $z = \Delta z$ ($z = 100$ m) in some parts of the dual-Doppler domain.

The trajectory calculations (to be presented in section 3), argue for having proxy wind data near to the ground owing to the fact that backward trajectories computed from low-level (e.g.,

*Corresponding author address: Mario Majcen, Department of Meteorology, Pennsylvania State University, 503 Walker Building, University Park, PA 16802; *e-mail*: mzm188@psu.edu

in the lowest few 100 m) vorticity maxima tend to originate between the lowest grid level ($z = 0$) and $z = \Delta z$ (trajectory calculations would not be very revealing without wind data at the lowest grid level because trajectories would terminate just a short distance backward from their origins due to the fact that air parcels arrive within vorticity maxima after rising abruptly from levels very near to the ground, i.e., below $z = \Delta z$). Horizontal winds at the lowest grid level (vertical wind velocity is zero at the lowest grid level) were approximated by extrapolating the synthesized horizontal wind field from the two grid levels above the lowest grid level. The wind components at the lowest grid level were parameterized such that the vertical shear between the lowest grid level and $z = \Delta z$ was some fraction of the shear between levels $z = \Delta z$ and $z = 2\Delta z$.

Prescribing the shears in the aforementioned layers to be equal is equivalent to prescribing a surface wind such that the horizontal wind speed increases linearly from the lowest grid level to $z = 2\Delta z$. Prescribing the shear in the layer extending from the lowest grid level to $z = \Delta z$ to be greater than the shear in the $z = \Delta z$ to $z = 2\Delta z$ layer approximates a logarithmic near-ground wind profile. For simplicity, the trajectories that will be shown in section 3 were obtained by prescribing the wind at the lowest grid level such that the horizontal wind speed increased linearly with height from the lowest grid level to $z = \Delta z$.

The sensitivity of the trajectories to the extrapolation method was evaluated by setting the vertical shear in the layer from z=0 to $z = \Delta z$ to be twice that in the layer from $z = \Delta z$ to $z = 2\Delta z$ (approximates a strongly logarithmic wind profile near the ground), as well as by defining the surface wind to be equal to the wind at $z = \Delta z$ (i.e., no shear in the $z = 0$ to $z = \Delta z$ layer). The trajectories using these two somewhat opposite extrapolation methods were not very different from those used to create the trajectories in section 3. After 5 minutes of integration, the trajectories computed using the various extrapolation techniques were all within 100 m of each other. The relative insensitivity of the trajectories to the extrapolation method is probably due to the presence of fairly weak shear in the $z = \Delta z$ to $z = 2\Delta z$ layer in this particular case.

Given the non-standard nature of this method, we will attempt to verify that it is appropriate to "fill in" low-level data in this manner.

3. Observations

The analyses of this case are in the earliest stages at the time of this writing. Nonetheless, within this section we attempt to summarize some of the noteworthy observations made thus far. Additional analyses and interpretations will be presented at the conference.

Figures 1–4 depict, at four different analysis times (2206:33, 2209:27, 2212:22, and 2215:45 UTC, repectively), horizontal cross-sections of equivalent reflectivity factor and near-ground horizontal wind, vertical velocity, and vertical vorticity, as well as some select storm-relative trajectories integrated backward in time from vertical vorticity maxima observed at 200 m.

Two prominent vorticity maxima intensify during the relatively short 9-min period from 2206–2215 UTC. The first of these attains its maximum intensity at 2209:27, at which time

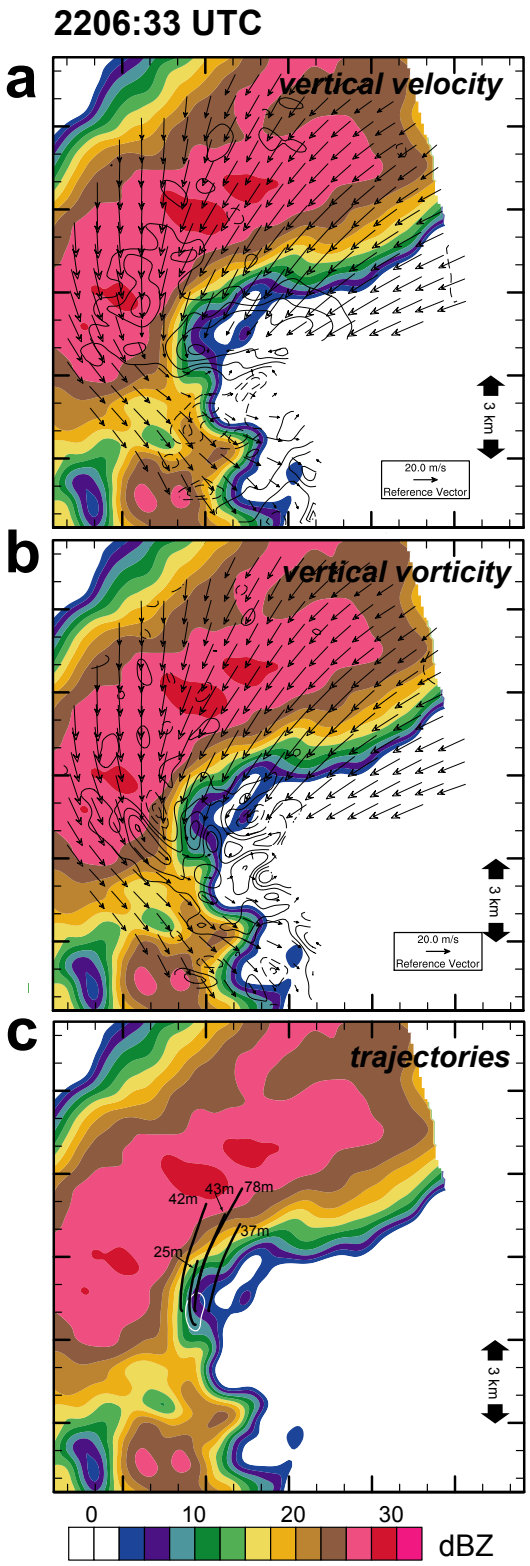

FIG. 1. (a) Horizontal cross-section of equivalent radar reflectivity factor (color shaded; see legend), vertical wind velocity (1 m s^{-1} contours, dashed contours denote negative values, 0 m s^{-1} suppressed for clarity), and storm-relative wind vectors at 200 m AGL for the 2206:33 UTC wind synthesis on 12 June 2004. (b) As in (a), but contours denote vertical vorticity (0.5 s^{-1} contour interval, dashed contours denote negative values, 0 s^{-1} is suppressed for clarity) (c) As in (a) but solid lines are trajectories integrated 3 minutes backward in time from the vorticity maxima at 200 m. Heights of the trajectories (AGL) at the end of integration are indicated. White contour denotes 1.5 s^{-1} vertical vorticity for orientation purposes.

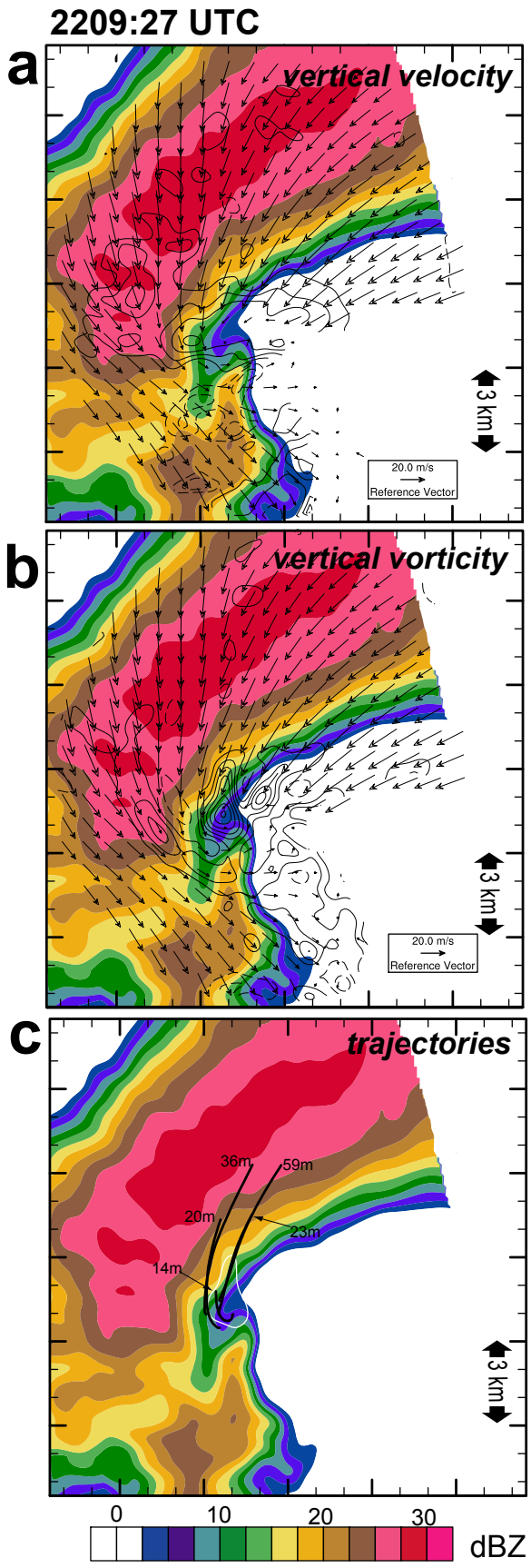

FIG. 2. As in Fig. 1, but for the 2209:27 UTC analysis time. Trajectories are integrated 5 minutes backward in time.

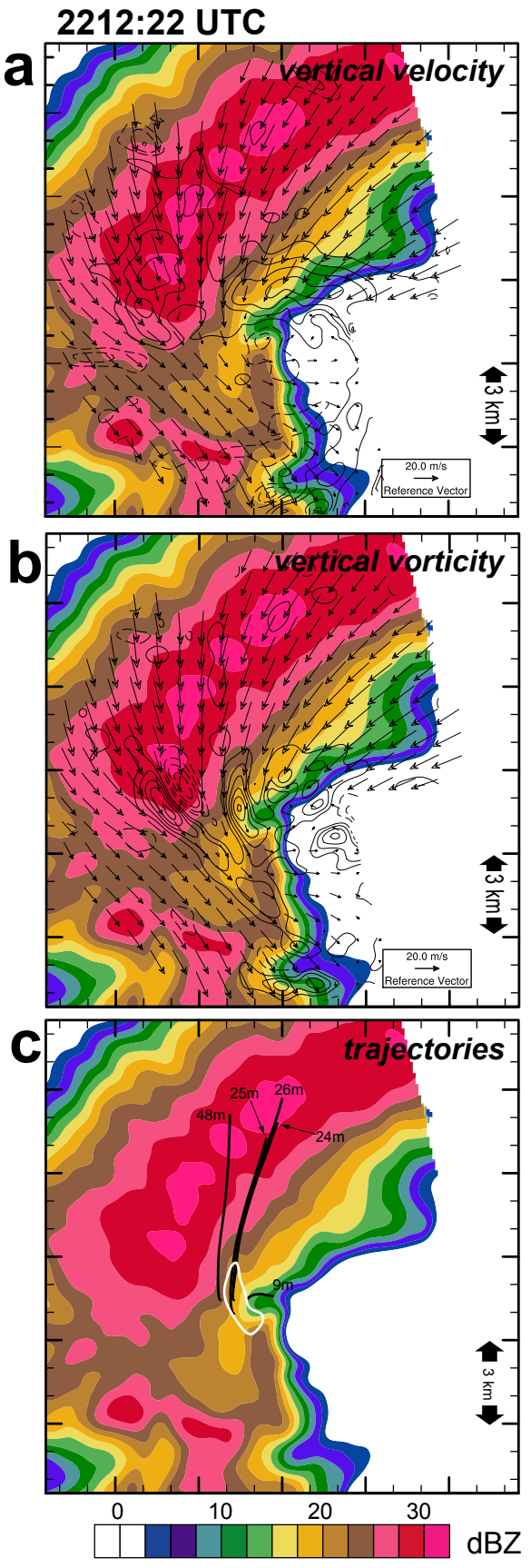

FIG. 3. As in Fig. 1, but for the 2212:22 UTC analysis time. Trajectories are integrated 5 minutes backward in time.

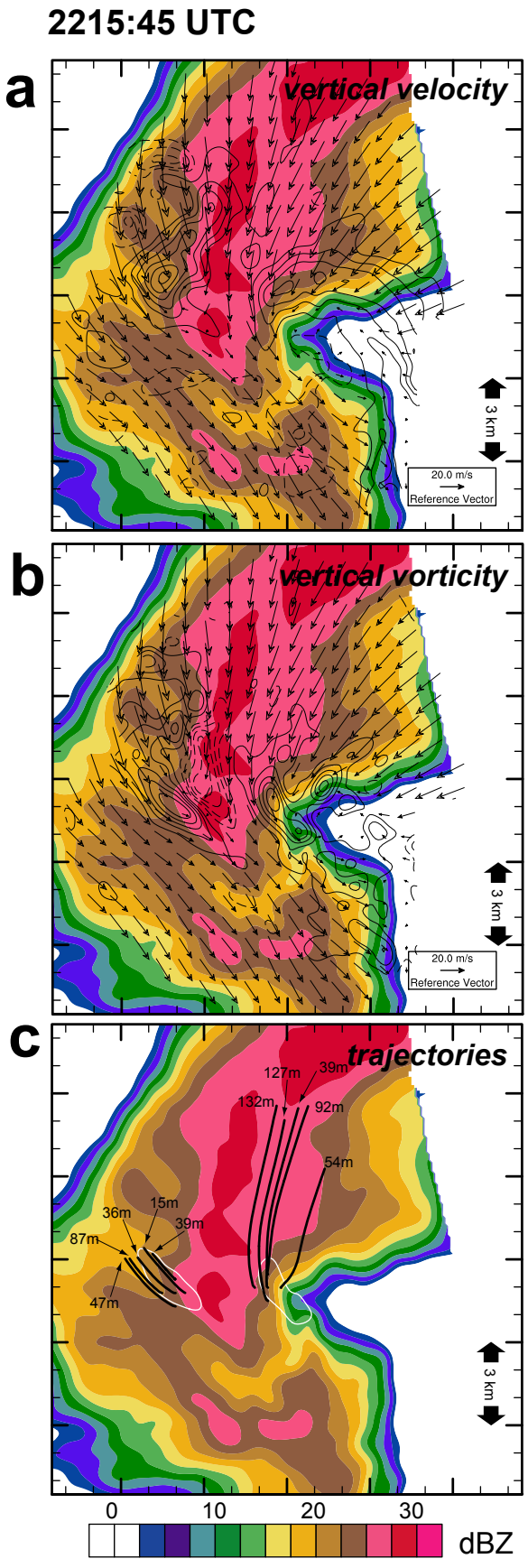

FIG. 4. As in Fig. 1, but for the 2215:45 UTC analysis. Trajectories are integrated 5 minutes backward in time.

the maximum vertical vorticity at 200 m exceeds 3.5×10^{-2} s^{-1} (Fig. 2b) At this time the storm exhibits many kinematic traits well-known to be associated with tornadic supercells (e.g., Brandes 1977, 1978; Ray et al. 1981) (Fig. 2): (1) the vorticity maximum lies within a large horizontal gradient of vertical velocity, but within updraft; (2) the gust front structure is occluded; (3) the updraft has a horseshoe-shaped appearance in a low-level horizontal cross-section; (4) an attendant vorticity minimum on the opposite side of the hook echo and rear-flank downdraft (RFD) as the vorticity maximum; (5) parcels of air entering the vorticity maximum have origins within the outflow/downdraft air mass, north of the circulation center [this finding also has been consistently made in high-resolution numerical simulation studies (e.g., Wicker and Wilhelmson 1995; Adlerman et al. 1999)].

A second vorticity maximum, located west of the maximum described above, intensifies rapidly between 2212 and 2215 UTC (Figs. 3b and 4b). It is in a somewhat peculiar location in that it intensifies to the west of the "stem" of the hook echo, well behind the leading portion of the outflow (and even behind the hook echo, with which the first vorticity maximum is related in a much more classic manner). The vorticity maximum has vertical and temporal continuity, and it is associated with prominent single-Doppler radial velocity signatures in both the DOW2 and DOW3 data; thus, the feature is almost certainly real and not an analysis artifact. This vorticity maximum attains a peak vorticity of 2.5×10^{-2} s^{-1} in the 2215:45 UTC analysis. It is associated with a rapidly intensifying updraft in this same approximate location as well, and, similar to the first vorticity maximum (and others documented historically in supercell thunderstorms), this vorticity maximum also is situated in a large horizontal gradient of vertical velocity.

4. Final comments and future work

In the upcoming months, the analysis of this case will include a much more detailed investigation of the mechanisms by which the vorticity maxima intensified and, if possible, the mechanisms that might have precluded additional amplification of vorticity into a tornado. Also, a multi-pass Barnes analysis technique will be developed and tested using available dual-Doppler radar datasets and synthetic radar datasets.

Acknowledgments. We wish to thank Dr. David Dowell for providing objective analysis and wind synthesis code, as well as the numerous ROTATE participants (too many to mention). Support from NSF grant ATM-0437512 and ATM-0437505 is also acknowledged.

REFERENCES

Adlerman, E. J., K. K. Droegemeister, R. Davies-Jones, 1999: A numerical simulation of cyclic mesocyclogenesis. *J. Atmos. Sci.*, **56**, 2045–2069.

Barnes, S. L., 1964: A technique for maximizing details in numerical weather map analysis. *J. Appl. Meteor.*, **3**, 396–409.

Brandes, E. A., 1977: Flow in a severe thunderstorm observed by dual-Doppler radar. *Mon. Wea. Rev.*, **105**, 113–120.

Brandes, E. A., 1978: Mesocyclone evolution and tornadogenesis: Some observations. *Mon. Wea. Rev.*, **106**, 995–1011.

Brandes, E. A., 1981: Finestructure of the Del City-Edmond tornadic mesocirculation. *Mon. Wea. Rev.*, **109**, 635–647.

Ray, P. S., R. J. Doviak, G. B. Walker, D. Sirmans, J. Carter, and B. Bumgarner, 1975: Dual-Doppler observation of a tornadic storm. *J. Appl. Meteor.*, **14**, 1521–1530.

Ray, P. S., J. B. Klemp, R. B. Wilhemson, 1981: Observed and numerically simulated structure of a mature supercell thunderstorm. *J. Atmos. Sci.*, **38**, 1558–1580.

Wicker, L. J., R. B. Wilhemson, 1995: Simulation and analysis of tornado development and decay within a three-dimensional supercell thunderstorm. *J. Atmos. Sci.*, **52**, 2675–2703.

Wurman, J. M., J. M. Straka, E. N. Rasmussen, M. Randall, and A. Zahrai, 1997: Design and deployment of a portable, pencil-beam, pulsed, 3-cm Doppler radar. *J. Atmos. Oceanic Technol.*, **14**, 1502–1512.